TECHNICAL REPORT ARCCB-TR-00011

# IMAGE PLATE X-RAY DIFFRACTION AND X-RAY REFLECTIVITY CHARACTERIZATION OF PROTECTIVE COATINGS AND THIN FILMS

S. L. LEE
D. WINDOVER
M. DOXBECK
T.-M. LU

JULY 2000

## US ARMY ARMAMENT RESEARCH, DEVELOPMENT AND ENGINEERING CENTER
### CLOSE COMBAT ARMAMENTS CENTER
### BENÉT LABORATORIES
### WATERVLIET, N.Y. 12189-4050

BENÉT LABS

APPROVED FOR PUBLIC RELEASE; DISTRIBUTION UNLIMITED

20000818 136

## DISCLAIMER

The findings in this report are not to be construed as an official Department of the Army position unless so designated by other authorized documents.

The use of trade name(s) and/or manufacturer(s) does not constitute an official endorsement or approval.

## DESTRUCTION NOTICE

For classified documents, follow the procedures in DoD 5200.22-M, Industrial Security Manual, Section II-19, or DoD 5200.1-R, Information Security Program Regulation, Chapter IX.

For unclassified, limited documents, destroy by any method that will prevent disclosure of contents or reconstruction of the document.

For unclassified, unlimited documents, destroy when the report is no longer needed. Do not return it to the originator.

# REPORT DOCUMENTATION PAGE

Form Approved
OMB No. 0704-0188

Public reporting burden for this collection of information is estimated to average 1 hour per response, including the time for reviewing instructions, searching existing data sources, gathering and maintaining the data needed, and completing and reviewing the collection of information. Send comments regarding this burden estimate or any other aspect of this collection of information, including suggestions for reducing this burden, to Washington Headquarters Services, Directorate for Information Operations and Reports, 1215 Jefferson Davis Highway, Suite 1204, Arlington, VA 22202-4302, and to the Office of Management and Budget, Paperwork Reduction Project (0704-0188), Washington, DC 20503.

| 1. AGENCY USE ONLY (Leave blank) | 2. REPORT DATE | 3. REPORT TYPE AND DATES COVERED |
|---|---|---|
| | July 2000 | Final |

**4. TITLE AND SUBTITLE**

IMAGE PLATE X-RAY DIFFRACTION AND X-RAY REFLECTIVITY CHARACTERIZATION OF PROTECTIVE COATINGS AND THIN FILMS

**5. FUNDING NUMBERS**

AMCMS No. 6111.02.H671.1

**6. AUTHOR(S)**

S.L. Lee, D. Windover (Benet and RPI, Troy, NY),
M. Doxbeck, and T.-M. Lu (RPI)

**7. PERFORMING ORGANIZATION NAME(S) AND ADDRESS(ES)**

U.S. Army ARDEC
Benet Laboratories, AMSTA-AR-CCB-O
Watervliet, NY 12189-4050

**8. PERFORMING ORGANIZATION REPORT NUMBER**

ARCCB-TR-00011

**9. SPONSORING / MONITORING AGENCY NAME(S) AND ADDRESS(ES)**

U.S. Army ARDEC
Close Combat Armaments Center
Picatinny Arsenal, NJ 07806-5000

**10. SPONSORING / MONITORING AGENCY REPORT NUMBER**

**11. SUPPLEMENTARY NOTES**

Presented at the 26th International Conference on Metallurgical Coatings and Thin Films, San Diego, CA, 12-15 April 2000.
Published in proceedings of the conference. To be published in *Thin Solid Films* or *Surface and Coatings Technology*.

**12a. DISTRIBUTION / AVAILABILITY STATEMENT**
Approved for public release; distribution unlimited.

**12b. DISTRIBUTION CODE**

**13. ABSTRACT (Maximum 200 words)**
Two-dimensional image plate applications in x-ray diffraction and x-ray reflectivity characterization, using grazing-incidence geometry and radiation from a conventional x-ray tube, were explored. X-ray diffraction and x-ray reflectivity data were obtained from a conventional diffractometer with Si(Li) detector. These data complement image plate results to give more complete phase and structure information. Protective chromium coatings, electrochemically deposited onto the bore of steel cylinders, were investigated. Retained austenite content in martensitic steel was measured in simulated, inside-diameter, bore geometry. This approach demonstrates the versatility of the method for nondestructive chemical analysis and phase differentiation of interior bore surfaces in piping structures. MATLAB-based processing software was developed to facilitate quantitative image analysis, including multiple $2\theta$ scans, $\chi$-plots, and pole figure reconstruction from multiple $\varphi$ images, where $\chi$ and $\phi$ designate, respectively, specimen tilt and rotation. In x-ray reflectivity applications, 12-nm tantalum and 80-nm tantalum oxide thin films sputtered on (100)-oriented silicon wafers were investigated. Density and thin-film thickness were obtained from specular reflectivity modeling involving the periodicity of the interference fringes. Two-dimensional Kiessig interference-fringe images were analyzed and compared to conventional specular x-ray reflectivity images for the measurement of thin-film thickness and thickness uniformity over a sample.

**14. SUBJECT TERMS**
Digital Film, Image Plate, Chromium, Tantalum, Tantalum Oxide, Austenite, Martensite, Coatings, Thin Films, X-Ray Diffraction, X-Ray Reflectivity

**15. NUMBER OF PAGES**

21

**16. PRICE CODE**

| 17. SECURITY CLASSIFICATION OF REPORT | 18. SECURITY CLASSIFICATION OF THIS PAGE | 19. SECURITY CLASSIFICATION OF ABSTRACT | 20. LIMITATION OF ABSTRACT |
|---|---|---|---|
| UNCLASSIFIED | UNCLASSIFIED | UNCLASSIFIED | UL |

NSN 7540-01-280-5500

Standard Form 298 (Rev. 2-89)
Prescribed by ANSI Std. Z39-18
298-102

# TABLE OF CONTENTS

## TABLES

## LIST OF ILLUSTRATIONS

## ACKNOWLEDGEMENTS

# INTRODUCTION

Since the discovery of x-rays by Roentgen in 1895 and x-ray diffraction by Von Laue in 1912, x-ray diffraction applications in the study of single crystals and polycrystalline aggregates continue to grow and flourish. Kiessig first observed x-ray reflectivity in 1931 (ref 1). Parratt developed Fresnel-based curve fitting for the technique in 1954 (ref 2), and recent, renewed interests led to its powerful utility in the analysis of thin films (ref 3). Early, Debye-Scherrer, Seeman-Bohlin, Guinier cameras, etc. utilized chemical photographic films, but fast, precise, reproducible, quantitative analysis was difficult to achieve, since the data were very dependent on the chemical developers and film sensitivity. In the development of sensor technology, one-dimensional position-sensitive proportional counters and array scintillation counters, and two-dimensional CCD cameras, and array proportional counters evolved. Thoms (ref 4) studied image plate characteristics for x-ray detection. Image plate Laue graphs were analyzed by Niimura et al. (ref 5) and Gibaud et al. (ref 6). Zontone et al. (ref 7) and Nishinaga et al. (ref 8) also performed image plate structure analyses using synchrotron radiation. Sasaki et al. (ref 9) measured residual stress distribution in coarse-grained polycrystalline materials using imaging plates. Recently, *in-situ* high-temperature x-ray diffraction measurements were taken using curved image plates to study thermal treatment of materials (ref 10).

Electrolytic chromium deposition at low temperature and current density, produces hard, brittle, high contraction (HC) chromium. Deposition at high temperature and current density in a flow-through tank produces a soft ductile, surface low contraction (LC) chromium with improved wear and erosion behavior (ref 11). The HC and LC chromium exhibit very different physical properties, such as hardness, brittleness, and residual stresses; and the texture effects of these properties are of interest (refs 12,13). For x-ray reflectivity applications, sputtered tantalum films were investigated because tantalum is a potential environment-friendly protective coating material for high-temperature pressure vessels (refs 14-16). It is also a potential diffusion barrier interconnect material for integrated circuit manufacturing (ref 17). Tantalum oxide films were investigated because tantalum oxide has been observed in fired, tantalum-coated barrels (ref 16), and it has applications as a high-dielectric material for capacitors. Energy-dispersive x-ray reflectivity was applied to study thin-film thickness and density in tantalum thin films and low-dielectric, spin-on, porous silicon dioxide films with densities as low as $1.1 \pm 0.1$ gm/cm$^3$ (refs 18,19).

Image plate x-ray diffraction provides fast simultaneous, multiple $2\theta$ scans at various $\chi$ tilts, while conventional x-ray diffraction scans provide only a single trace of $2\theta$ scan at a specified $\chi$. Versatile and fast image plates possess excellent $\theta$ and $\chi$ resolution without detector motion or specimen tilts. They are erasable, reusable, flexible, and may be cut into variable sizes. They have a high dynamic range and require no wet chemistry processing or attached bulky electronics, thus allowing them to fit into difficult structures, such as the interior of piping structures. They are also inexpensive compared to their two-dimensional counterpart, the area detector. In this work, an image plate detector complemented by a conventional Si(Li) detector was used for x-ray diffraction analysis of chromium protective bore coatings and x-ray reflectivity analysis of electronic thin films. Chromium coatings were electrodeposited onto the bore of 120-mm inside-diameter cylinders. The ~125-μm-thick, electrolytic, HC chromium coatings showed very strong <111> fiber texture, while the LC chromium showed more

randomly-oriented crystallites. Our x-ray diffraction determination of retained austenite in martensitic steel simulated the 120-mm inside-diameter geometry. It demonstrated that the method could be implemented for nondestructive chemical analysis inside a cylindrical structure. Conventional x-ray reflectivity was used to analyze the density and thickness of sputtered tantalum and $TaO_x$ thin films on (110)-oriented silicon wafers. A two-dimensional, image plate Kiessig interference image further allowed the study of thin-film thickness, surface, and interface uniformity across the specimen surface.

## IMAGE PLATE EXPERIMENTAL METHOD

Sealed-tube, x-ray sources with copper and chromium anodes and both long-focus and point-focus geometry, operating in the range of 1000 to 1600 watts, provided the radiation for the conventional and image plate x-ray diffraction and x-ray reflectivity studies. Conventional texture and reflectivity analyses were performed using a 4-axis, Scintag diffractometer with a $\theta$-$2\theta$ goniometer and a Kevex, Peltier-cooled, Si(Li) detector. For conventional pole figures, in-house texture software allows 1° or 2° $\chi$ and $\phi$ resolution instead of the 5° conventional system resolution. For image plate applications, BAS III image plates with a pixel size as small as 25 $\mu$m were used. A Fuji BAS-2500 Bio-Imaging Analyzer and an IP Eraser and a Power Macintosh PC were used for data processing. For the image plates to form an image, a europium ion trapped in a phosphor matrix is excited to a metastable state by an incident x-ray. This excited state is then harmonically released by a laser during a scanning process to produce a latent phosphor image that is then transferred digitally to a computer by a scanner. This phosphor image provides dynamic range over seven orders of magnitude. Current scanning techniques limit effective dynamic range to five orders of magnitude. Calibration of the image plate geometry, to convert from mm in plate to angles of $2\theta$, were performed using National Institute of Standards and Technology (NIST) corundum and chromium powder standards and $K_\alpha$ and $K_\beta$ radiation.

## GRAZING-INCIDENCE X-RAY DIFFRACTION AND X-RAY REFLECTIVITY

Figure 1a shows the grazing-incidence geometry used for x-ray diffraction analysis in this study, where $\phi$ is the rotation of the sample, required to emulate $\phi$-axis of conventional pole figures, and $\chi$ rotations on the plate image correspond to $\chi$-axis of traditional pole figure data. The grazing-incidence angle is noted by the specimen tilt $\omega$ with respect to the incident x-ray beam. The grazing-incidence geometry was chosen to promote surface analysis, since grazing-angle x-rays provide more surface penetration. However, the technique is applicable to study surfaces of both bulk coatings as well as ultra-thin films. A conventional copper anode x-ray source, operating at 40 kV and 40 mA was collimated using a 1-mm-round source orifice near the tube (~24-mm from the source) and a 1-mm refining round orifice located close to the sample (~20-mm from the sample). The entire source-to-sample path was 286-mm. The thermal focal spot 0.4-mm × 8-mm x-ray anode was rotated 90° to provide an approximately 0.8-mm × 0.4-mm optical point source. For grazing-incidence x-ray diffraction analysis, a grazing angle of 10° was used for all images presented. In-house interactive MATLAB software was developed for texture image processing. The algorithm involved fitting the curvature of the Debye rings to a fourth-order polynomial and construction of a curved window to extract desired intensity

information. The window, by sampling the whole range of activated pixels, automatically takes into account dispersion effects due to geometry.

X-ray reflectivity is a nondestructive, noncontact technique applicable to single and multi-layer crystalline, amorphous, and liquid-layer thin films. The most common form of this technique involves specular reflection, where incident and outgoing angles are kept equal by

$$\theta = \theta_{incident} = \theta_{outgoing} \tag{1}$$

This geometry keeps all scattering information, related in reciprocal-space to inverse distances, perpendicular to the surface (parallel components are zero) and is related to wavelength and angle by the standard diffraction relation

$$k_\perp = \frac{4\pi}{\lambda} \cdot \sin(\theta) \tag{2}$$

For conventional x-ray reflectivity analysis on the Scintag diffractometer, small angle scans up to 5° 2θ were performed using copper and chromium tubes at 10 kV and 10 mA for primary patterns, and 30 kV and 30 mA to highlight the oscillatory tail data (this higher-energy saturates the detector at low angles). Figure 1b shows the geometry of the image plate reflectivity collection. The image plate remains fixed while the sample is tilted through a range of angles in ω (defined by side top view in Figure 1a). Fast Fourier transforms were used to find periodicity in the x-ray reflectivity signals, as well as in Parratt model fits.

## CHEMICAL ANALYSIS SIMULATING IN-BORE GEOMETRY

Figure 1c shows the simulated inside-diameter cylinder geometry for x-ray diffraction chemical analysis. Both tube and image plate must fit within the cylinder, and x-rays must be focused onto a small section of the tube surface. For preliminary efforts in this project, the well-known problem of retained austenite in martensitic steel was imaged within the bore dimension constraints. For content of retained austenite in martensite analysis, two NIST calibration standards containing 2% and 33% austenite in ferrite-martensite were used. For the inside-diameter bore analysis, a small x-ray tube (~40-mm diameter including collimators) with a chromium anode was used. The tube, collimators, and film detector fit inside a section of a steel 120-mm-diameter cylinder. The small chromium x-ray tube operated at 100 watts of power.

## ANALYSIS OF ELECTROCHEMICAL-DEPOSITED CHROMIUM COATINGS

High contraction chromium coating was deposited onto steel cylinders of 120-mm diameter at 55°C bath temperature, 30 amp/dm$^2$, and plating solution of $CrO_3$, $H_2SO_4$ plus distilled water. Figure 2a shows the image plate results of HC chromium coating on steel (region 1 gives wedge-shaped sample imprint) obtained using a nickel-filtered, copper, point-source-configured, x-ray tube with a scan time of one minute and two round 1-mm collimators to reduce divergence. Figure 2b depicts the corresponding analysis of traces at χ = 0°, +/-35.3°, +/-54.7°. Film background intensity subtraction was performed using a fourth-order curve fit to the image

data. The raw distance, in mm, was shown, which can be converted to $2\theta$ using both chromium powder calibration and computed geometric calibration. The (110) reflection appears as two dots (region 2 in Figure 2a denotes the upper dot) with strong intensity at $\chi = 35°$, the (200) reflections appear as weaker dots (region 3 in Figure 2a denotes the upper dot) at $\chi = 55°$. The results led us to conclude that this specimen possesses strong body-centered-cubic (bcc) chromium <111> texture. Figure 2c depicts the grazing-incidence image plate results of LC chromium coatings plated at a higher bath temperature and a higher current density in a flow-through plating bath, consisting of the same chemical concentrations. The figure shows a nearly uniform circle of the (110) reflection. This indicates near-random orientation of crystallites in this specimen. The corresponding traces, not shown here, gave equal intensity peaks for all $\chi$ within the range, including $\chi = 0°$, +/-35.3°, +/-54.7°. Figure 2d shows the interactive MATLAB-generated window for the analysis of the Debye rings superimposed on a planar magnetron-sputtered test tantalum coated specimen. The three Debye rings from left to right shown in the figure represent respectively, the (110), (200), and (211) reflections.

Figure 2e shows a reconstructed (110) pole figure of HC chromium obtained using image plates shot at ten different $\phi$ angles. This figure shows the fiber nature of the texture with good azimuth symmetry. Figure 2f shows a conventional (110) pole figure for HC chromium using 2° by 2° resolution plotted on the same scale for direct comparison. Both methods reveal the fiber nature of bcc chromium in the HC chromium specimen. Figure 2g shows a conventional (110) pole figure for LC chromium using 2° by 2° resolution. The figure shows weak <111> fiber texture with greatly broadened full-width at half maximum, representing the near-random oriented crystallites in this specimen. The contrast between Figures 2f and 2g thus shows the difference from a highly-textured to a near-random specimen.

Figure 2h shows the $\chi$-plots for HC and LC chromium along the (110) reflection extracted from the image plate data using MATLAB software. High contraction chromium showed a tight fiber component, while LC chromium showed a near-random orientation from the flat $\chi$-plot. In this figure, the image plate x-ray diffraction data were also compared with conventional x-ray diffraction data, showing minor discrepancies. The open circles and triangles represent conventional x-ray diffraction data. The closed diamonds and crosses represent image plate x-ray diffraction data. Conventional pole figure data collection requires tilting the specimen out of the plane of reflection during data collection, introducing large intensity variations in pole figures. The image plate collection method does not require specimen tilt, removing this intensity error from data collection. The LC $\chi$-plots show the intensity fall-off at higher $\chi$ tilts, caused by the defocusing and absorption, even after corrections using the powder method were applied to the data. The correlation of structure to the difference of physical properties in HC and LC chromium is listed in Table 1. While highly-textured HC chromium is hard, brittle, with high tensile residual stresses, LC chromium is soft, ductile, with low level of tensile residual stresses.

## ANALYSIS OF SPUTTERED TANTALUM AND TANTALUM OXIDE THIN FILMS

The x-ray refractive index in materials is typically a number slightly less than one. Total reflection occurs when the x-ray incident angle is smaller than the critical angle, $\theta_c$. For angles

greater than the critical angle, the reflectivity rapidly falls off, proportional to $k_\perp^{-4}$ and oscillations in the data (Kiessig fringes) result from the interference of partially reflected and transmitted x-rays within the sample layers. From the critical angle, the periodicity and intensity variations in the x-ray reflectivity data, the thin-film density, and thickness can be determined. The reflectivity pattern produced is an average of thickness, density, and roughness information in the X-direction, but provides a profile of the thickness in the Y-direction, which could be exploited in the measurement of graded thickness films. Conventional reflectivity averages in both the X- and Y-directions. By keeping the plate fixed and available for scattering throughout the ω-tilt range, the plate geometry collects both specular and off-specular reflectivity data simultaneously, which tends to "wash" the resolution of the oscillations. The oscillations are still visible, however, since specular reflectivity is typically orders-of-magnitude more intense than off-specular reflectivity, therefore dominating the picture.

Figure 3a shows the grazing-incidence image plate results for the planar magnetron-sputtered tantalum thin film on a (100) silicon wafer. Region 1 depicts the intensity saturation of the film plates; region 2 depicts the oscillations associated with thickness and the oscillation uniformity. Figure 3b shows the grazing-incidence image plate results for the planar magnetron-sputtered tantalum oxide thin film on a (100) silicon wafer obtained under the same experimental conditions. Region 1 indicates plate intensity saturation, and region 2 indicates the oscillation pattern yielding thickness. The uniform two-dimensional Kiessig interference image across the surface of the films (region 2) revealed a fairly uniform thin-film surface, interface, and thickness. Fourier transform shows that the lower periodicity in Figure 3a resulted in a film thickness of 12-nm, compared to Figure 3b, which resulted in a film thickness of 82-nm.

Figure 3c shows the x-ray reflectivity analysis of the tantalum oxide. The top curve shows the Parratt-based, best-fit model of the reflectivity curves. Scintag reflectivity software was used for the model fit. The analyses resulted in a $TaO_x$ film density of 7 $gm/cm^3$, film thickness of 81.9-nm, and film roughness of 0.65-nm, assuming a silicon density of 2.33 $g/cm^3$ and roughness of 0.85-nm. The middle curve shows the data from conventional specular x-ray reflectivity using a one-dimensional detector. The lower curve shows a digital image plate profile. The "washed" nature of the image plate oscillations is due to the "total reflectivity" collection properties of the image plate, where specular and off-specular data are collected simultaneously. Thickness determination from the Parratt fit and from Fourier analysis of both conventional and image plate periodicity of the curves resulted in an average film thickness of ~82-nm.

## AUSTENITE IN FERRITE-MARTENSITE ANALYSIS IN A CYLINDER BORE

Versatile image plates have a potential use for in-bore chemical analysis of piping structure. Two NIST standards containing 2% and 33% austenite in ferrite-martensite were placed inside a steel cylinder of 120-mm inside diameter to demonstrate image plate capability of chemical analysis within the bore. Martensite, with a body-centered tetragonal structure, is the interstitial solid solution of carbon in α-iron. Austenite is an interstitial solid solution of carbon in face-centered-cubic (fcc) γ-iron. Hardening of steel requires heating to high temperature to form austenite, then quenching to room temperature to transform to a hard metastable, martensitic phase. Incomplete transformation resulting in retained austenite in martensitic steel

(111) (region 1), $\alpha$-iron (110) (region 2), $\gamma$-iron (200) (region 3) present. Figure 4b shows an image of the 2% austenite specimen with only the bcc $\alpha$-iron (110) line present. Figure 4c shows a comparison of the digital image plate profiles of the austenite content samples at $\chi = 0°$. Both images were taken with sample-to-source and sample-to-plate distances of approximately 40-mm using $K_\alpha$ radiation from a chromium tube. From the intensity of the fcc $\gamma$-iron (111) and $\gamma$-iron (200) relative to the bcc $\alpha$-iron (110), content of austenite in martensite can be determined and agreed with the NIST specified values. This treatment of retained austenite in martensite is under the assumption that no other phases are present in the specimens and assumes that both phases are relatively free of texture as specified by the ASTM standard (ref 20) on retained austenite determination in steel.

## CONCLUSION

This work explored grazing-incidence x-ray diffraction and x-ray reflectivity techniques using digital image plates and a conventional laboratory x-ray source. The techniques revealed unique applications in protective coating and thin-film characterization as follows:

1. Image plate x-ray diffraction complements conventional x-ray diffraction to allow fast and more complete chemical, phase, and structural analysis of crystalline solids. Our results demonstrated that the techniques provided a fast, quantitative method of structural differentiation of HC and LC chromium protective coatings.

2. Image plate x-ray diffraction analysis inside a cylinder bore was demonstrated by determining retained austenite content in ferrite-martensite steel using a chromium x-ray tube that fit inside a cylinder.

3. X-ray reflectivity is a relatively new development for ultra-thin films and multi-layer thin-film property measurements, such as thin-film density, thickness, and roughness. This work demonstrated that two-dimensional image plate x-ray reflectivity could provide a fast, new method to measure film thickness and screen for thin-film surface and interface uniformity.

In the future, image plate x-ray diffraction inside a cylinder can be used to nondestructively measure the phase contents of multiple-phase specimens incorporating preferred orientation, e.g., $\alpha$- and $\beta$-phase tantalum coatings. This would be a valuable tool for the development of future protective bore coatings. Furthermore, a coupled x-ray diffraction and x-ray reflectivity technique has the potential for nondestructive surface analysis inside pressure vessels before and after operation. The identification of chemical species produced due to tube/projectile interactions can help in understanding wear and erosion and ensure the reliable operation of pressure vessels. Image plate x-ray diffraction and x-ray reflectivity have the potential for *in-situ* protective coatings and film analyses during film deposition and growth.
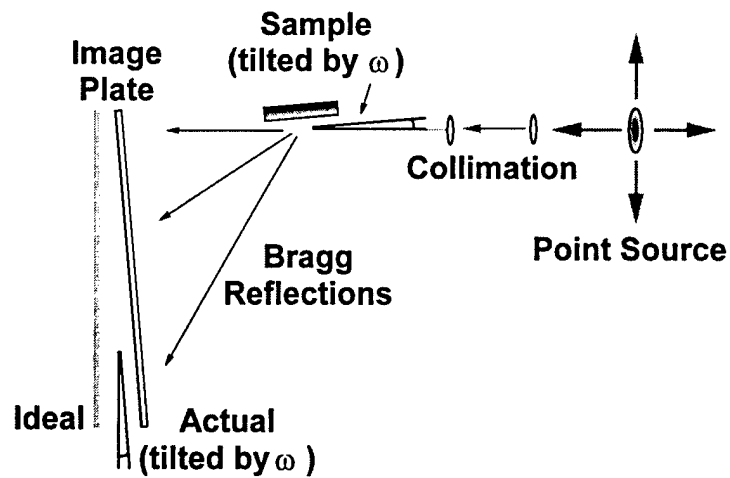
# REFERENCES

1. Kiessig, H., *Ann. Phys.*, Vol. 10, 1931 p. 769.

2. Parratt, L.G., *Physical Review*, Vol. 95, 1954, p. 359.

3. Chason, E., and Mayer, T.M., *Critical Reviews in Solid State and Materials Sciences*, Vol. 22, 1997, p. 1.

4. Thoms, M., *Nuclear Instruments and Methods in Physics Research, Section A*, Vol. 389, 1997, p. 437.

5. Niimura, N., Minezaki, Y., Nonaka, T., Castagna, J.-C., Cipriani, F., Hoghoj, P., Lehmann, M.S., and Wilkinson, C., *Nature Structural Biology*, Vol. 4, 1997, p. 909.

6. Gibaud, A., Harlow, D., Hastings, J.B., Hill, J.P., and Chapman, D., *Journal of Applied Crystallography*, Vol. 30, 1997, p. 16.

7. Zontone, F., D'Acapito, F., and Gonella, F., *Nuclear Instruments and Methods in Physics Research, Section B*, Vol. 147, 1999, p. 416.

8. Nishinaga, T., Nishioka, K., Harada, J., Sasaki, A., and Takei, H., *Advances in the Understanding of Crystal Growth Mechanisms*, Elsevier Science, 1997.

9. Sasaki, T., Yazawa, K., and Hirose, H., *Journal of the Society of Materials Science, Japan*, Vol. 48, 1999, p. 1431.

10. Pickup, D.M., Mountjoy, G., Roberts, M.A., Wallidge, G.W., Newport, R.J., and Smith, M.E., *Journal of Physics: Condensed Matter*, Vol. 12, 2000, p. 3521.

11. Chen, E.S., "Improved Electrodeposited Low Contraction Chromium," Technical Report ARLCB-TR-82009, Benet Laboratories, Watervliet, NY, April 1982.

12. Lee, S.L., Windover, D., and Mello, K., *Advances in X-Ray Analysis*, Vol. 41, 1999, p. 707.

13. Lee, S.L., and Capsimalis, G., *Advances in X-Ray Analysis*, Vol. 39, 1997, p. 255.

14. Matson, D.W., Merz, M.D., and McClanahan, E.D., *Journal of Vacuum Science and Technology A*, Vol. 10, No. 4, 1992, p. 1791.

15. Lee, S.L., and Windover, D., *Surface and Coatings Technology*, Vol. 108-109, 1998, p. 65.

16. Lee, S.L., Cipollo, M., Windover, D., and Rickard, C., *Surface and Coatings Technology*, Vol. 120-121, 1999, p. 44.

17. Catania, P., Doyle, J.P., and Cuomo, J.J., *Journal of Vacuum Science and Technology A*, Vol. 10, No. 5, 1992, p. 3318.

18. Windover, D., Barnat, E., Kim, J.Y., Nielsen, M., Lu, T.-M., Kumar, A., Bakhru, H., Jin, C., and Lee, S.L., *Advances in X-Ray Analysis*, Vol. 42, 2000, p. 590.

19. Windover, D., Lu, T.-M., Lee, S.L., Kumar A., Bakhru, H., Jin, C., and Lee, W., *Applied Physics Letters*, Vol. 76, No. 2, 2000, p. 158.

20. ASTM Standard E975-95, American Society for Testing and Materials, West Conshohocken, PA, 1995.

**Table 1. Properties in Electrolytic HC and LC Chromium**

| Properties | HC Chromium | LC Chromium |
|---|---|---|
| Physical Appearance | Shiny | Dull |
| Preferred Orientation | (111) | Near-Random |
| Texture | Tight Fiber Texture | Very Broad Fiber Texture |
| Knoop Hardness | 1005 ±52.9 | 527.1 ±22.8 |
| Vertical and Lateral Cracks | Yes | None or Few |
| Ductility | Brittle | Ductile |
| Thermal Contraction | Shrink after Heating | Negligible Contraction after Heating |
| Surface Residual Stress | High Tensile | Low Tensile |

# Top View

**Image Plate**

**Sample (tilted by $\omega$)**

**Collimation**

**Point Source**

**Bragg Reflections**

**Ideal**

**Actual (tilted by $\omega$)**

# Side View

**Image Plate**

**Sample (rotated by $\phi$)**

$\chi$

$\phi$

**Collimation**

**Point Source**

**Bragg Reflections**

**Rotations on Plate Correspond to Pole Figure $\chi$**
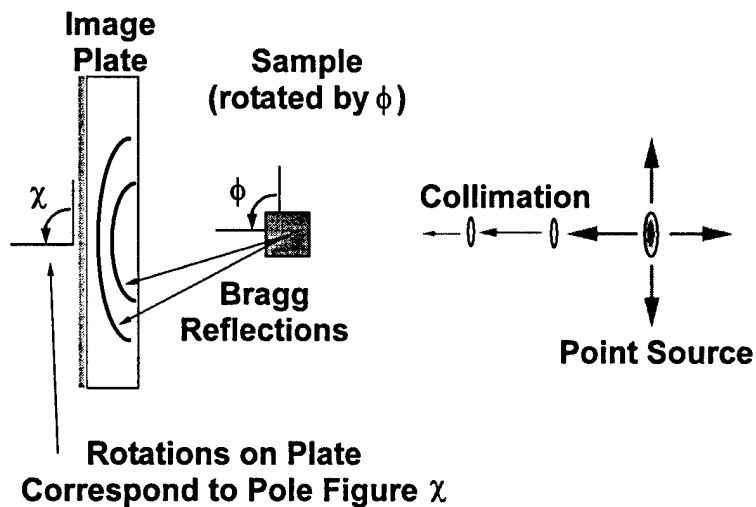
Figure 1a. Geometry used for grazing-incidence image plate x-ray diffraction studies comparing the sample orientation to the various angles used in image plate analysis and pole figure analysis.

## Side View

**Image Plate**

**Sample**

**Collimation**

Y

Y

**Line Source**

X

**Reflectivity Oscillations**
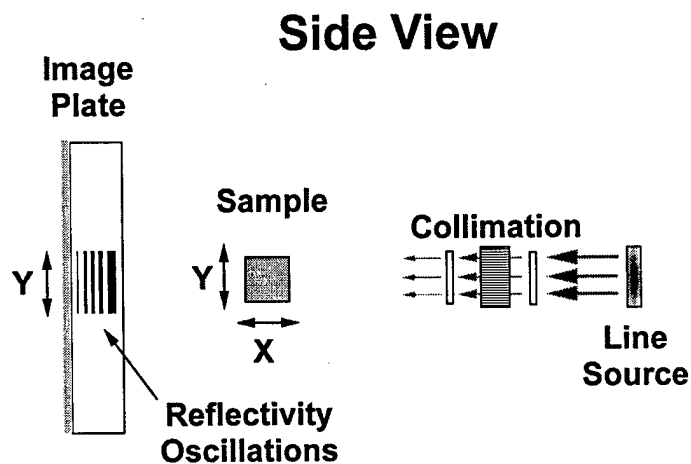
Figure 1b. Geometry used for x-ray reflectivity studies showing the plate geometry, pattern orientation, and sample axes.

## Side View

### Simulated Cylinder Bore Geometry

**Bragg Reflections**

**X-ray Source**

**Image Plate**

**(area being analyzed)**
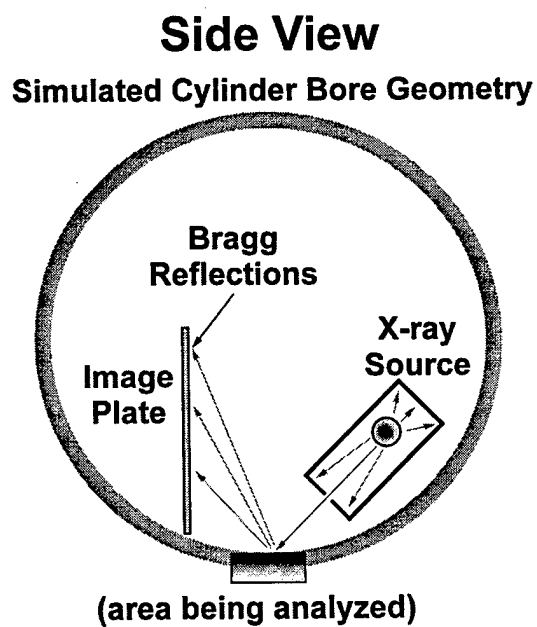
Figure 1c. Simulated geometry for nondestructive chemical analysis inside the bore of a cylindrical structure.
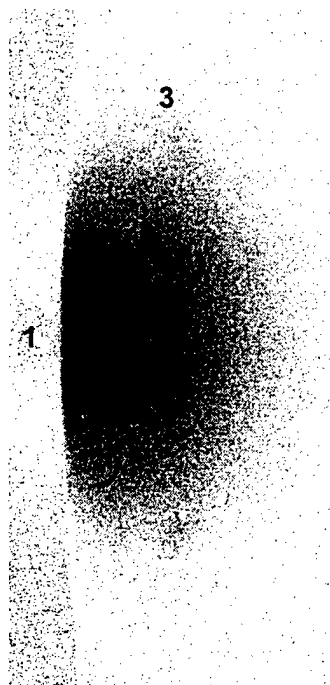
Figure 2a.  HC chromium coatings using
digital image plate and a copper x-ray tube.
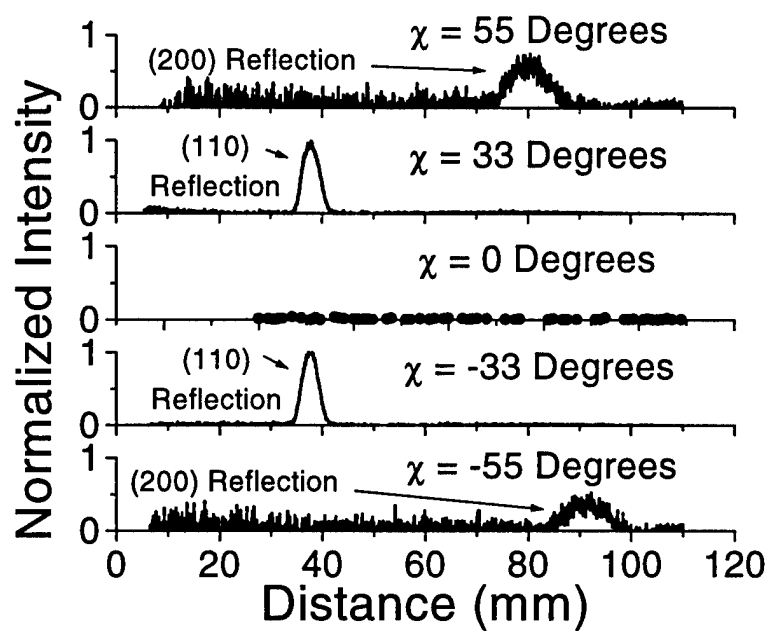


Figure 2b.  HC chromium image plate analysis of traces at $\chi = 0°$, $\pm35.3°$, $\pm54.7°$.
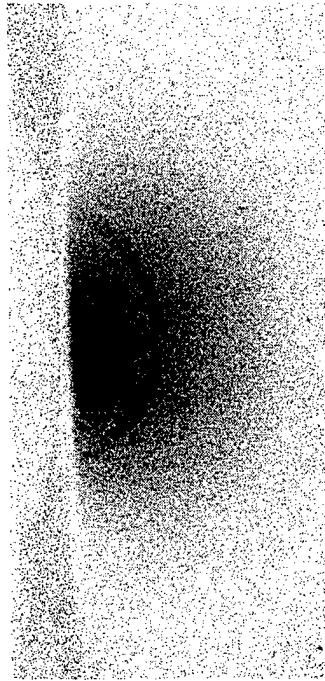
Figure 2c.  LC chromium coatings using
digital image plate and a copper x-ray tube.
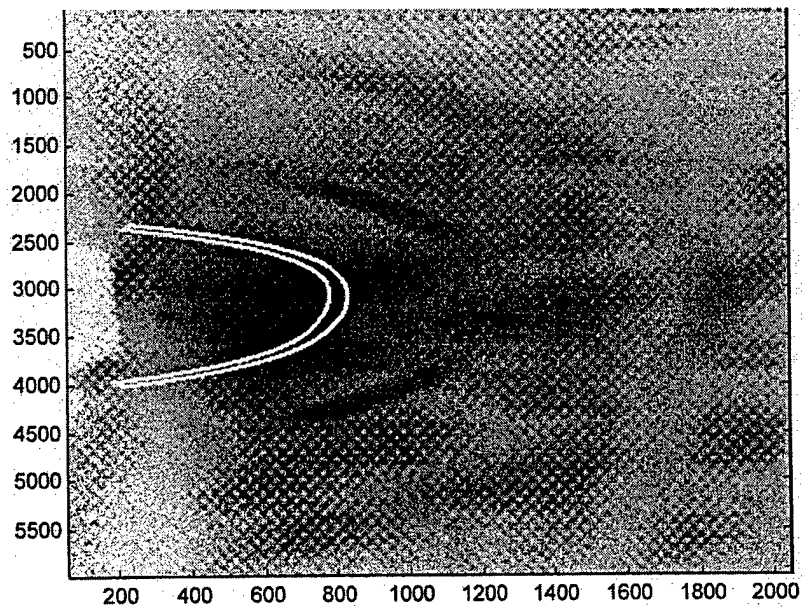


Figure 2d.  MATLAB-generated window for the analysis of Debye
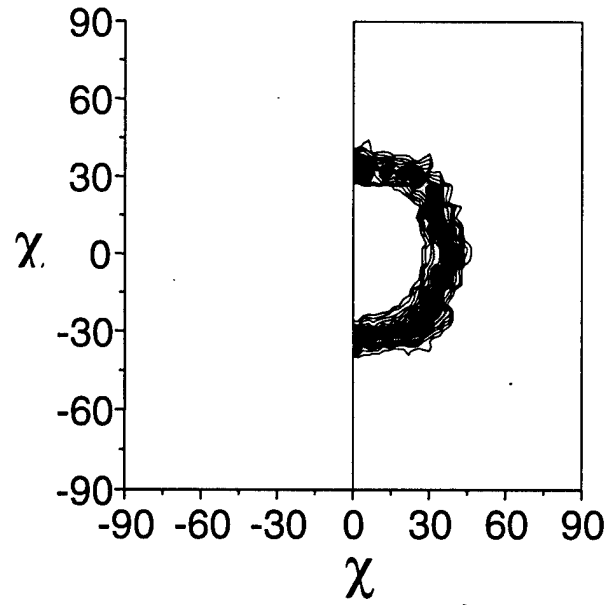rings superimposed on an image for a sputtered tantalum specimen.

13

Figure 2e. Reconstructed (110) pole figure of HC chromium from images obtained from ten φ angles from 0° to 90°, showing the fiber nature of the texture.
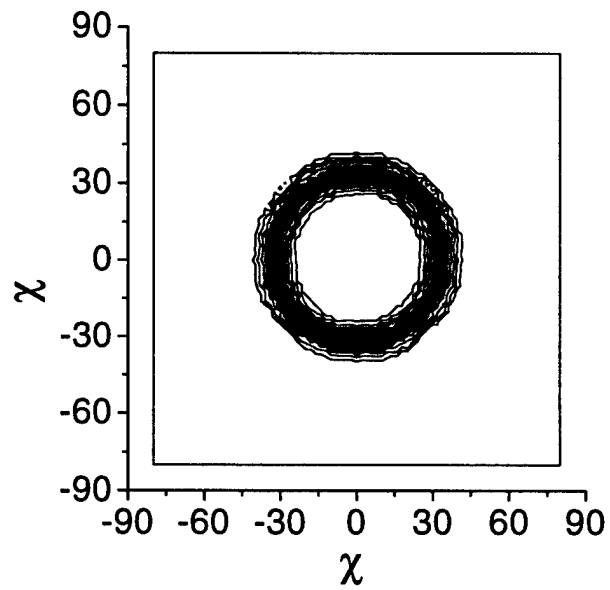


Figure 2f. Conventional (110) pole figure for HC chromium using 2° by 2° resolution plotted to the same dimension as Figure 2e, showing fiber texture.
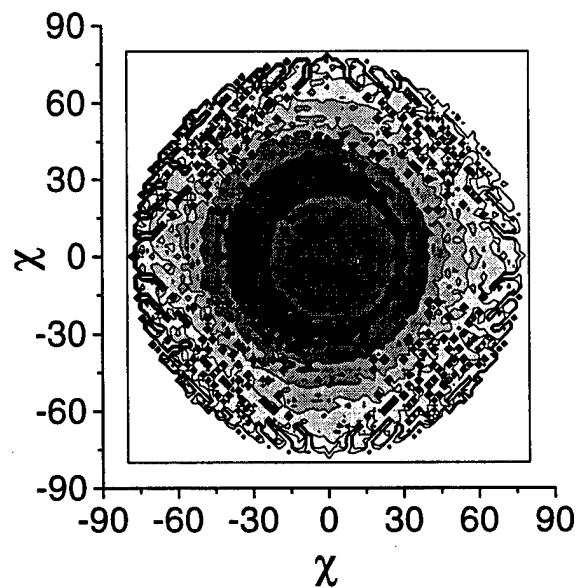
Figure 2g. Conventional (110) pole figure for LC chromium using
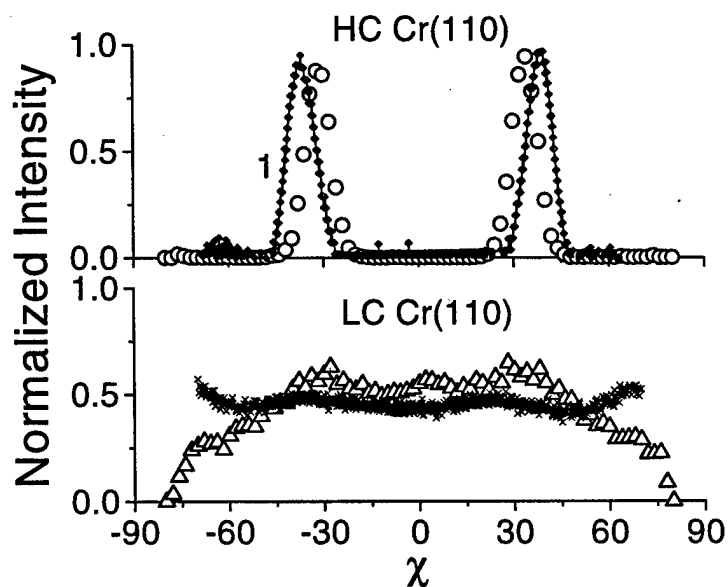2° by 2° resolution, showing the randomness of the specimen.



Figure 2h. χ-plots for HC and LC chromium along the (110) reflection
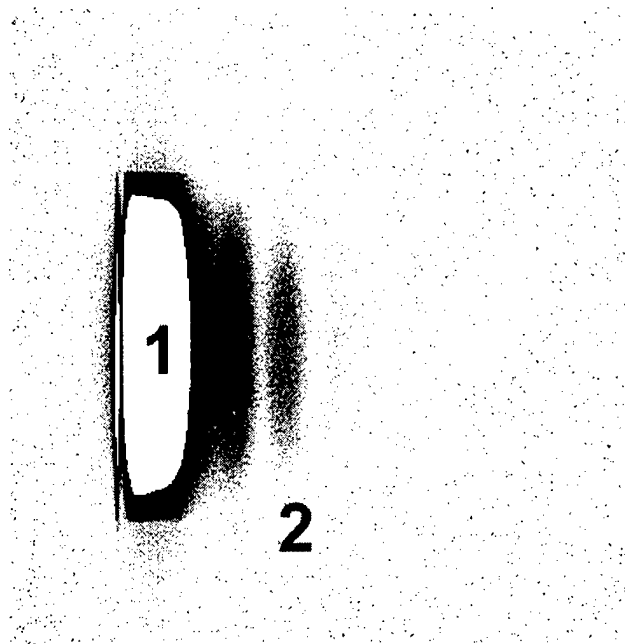extracted from the image plate data using MATLAB software.

Figure 3a. Grazing-incidence image plate of planar magnetron-sputtered 120 Å-thick tantalum thin film on (100) silicon substrate.
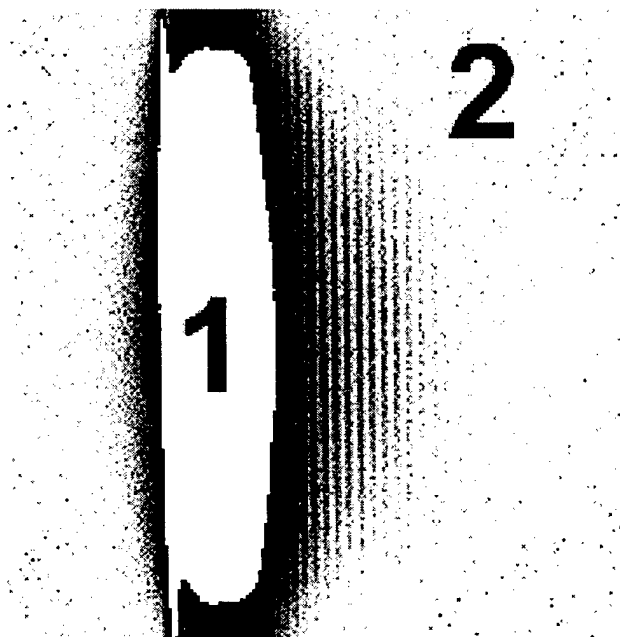


Figure 3b. Grazing-incidence image plate of planar magnetron-sputtered 820 Å-thick tantalum oxide thin film on (100) silicon substrate.
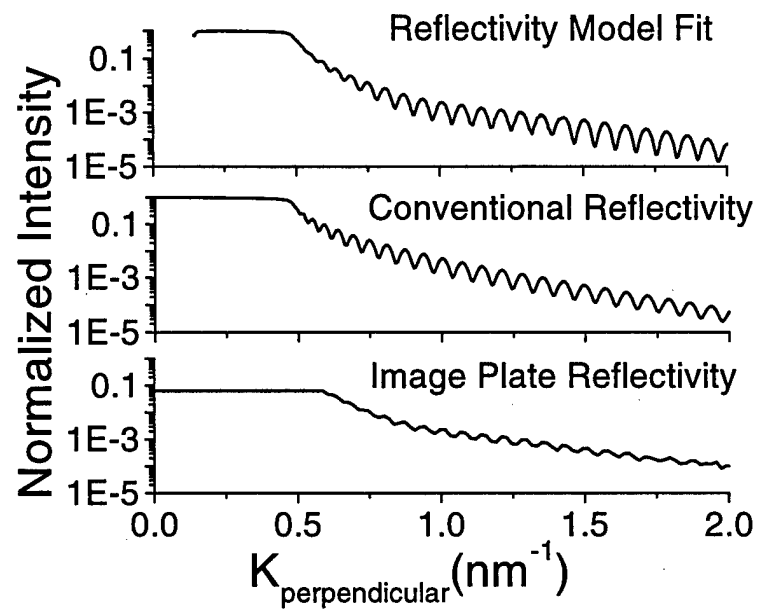
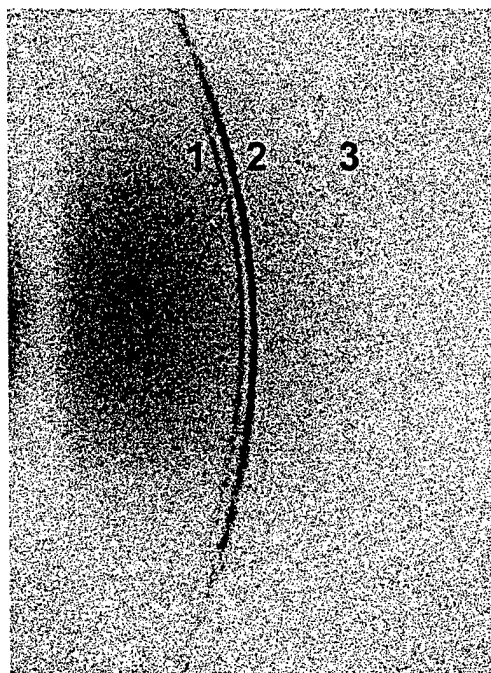Figure 3c. X-ray reflectivity analysis of the tantalum oxide.



Figure 4a. Image plate of a 33% austenite in ferrite-martensite specimen using a chromium x-ray tube inside a cylinder.
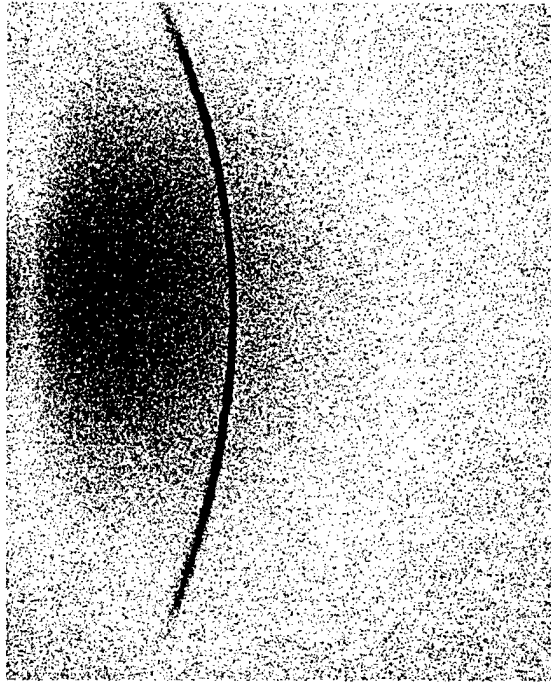
17

Figure 4b. Image plate of a 2% austenite in ferrite-martensite
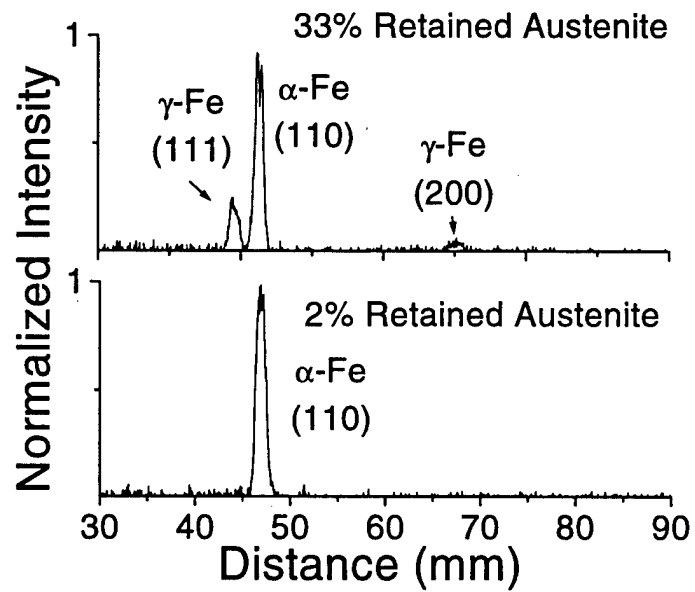specimen using a chromium x-ray tube inside a cylinder.



Figure 4c. Comparison of image plate analysis of traces from 2%
and 33% austenite in ferrite-martensite specimens taken at $\chi = 0°$.

# TECHNICAL REPORT INTERNAL DISTRIBUTION LIST

|  | NO. OF COPIES |
|---|---|
| TECHNICAL LIBRARY<br>ATTN: AMSTA-AR-CCB-O | 5 |
| TECHNICAL PUBLICATIONS & EDITING SECTION<br>ATTN: AMSTA-AR-CCB-O | 3 |
| OPERATIONS DIRECTORATE<br>ATTN: SIOWV-ODP-P | 1 |
| DIRECTOR, PROCUREMENT & CONTRACTING DIRECTORATE<br>ATTN: SIOWV-PP | 1 |
| DIRECTOR, PRODUCT ASSURANCE & TEST DIRECTORATE<br>ATTN: SIOWV-QA | 1 |

NOTE: PLEASE NOTIFY DIRECTOR, BENÉT LABORATORIES, ATTN: AMSTA-AR-CCB-O OF ADDRESS CHANGES.

# TECHNICAL REPORT EXTERNAL DISTRIBUTION LIST

| | NO. OF COPIES | | NO. OF COPIES |
|---|---|---|---|
| DEFENSE TECHNICAL INFO CENTER<br>ATTN: DTIC-OCA (ACQUISITIONS)<br>8725 JOHN J. KINGMAN ROAD<br>STE 0944<br>FT. BELVOIR, VA 22060-6218 | 2 | COMMANDER<br>ROCK ISLAND ARSENAL<br>ATTN: SIORI-SEM-L<br>ROCK ISLAND, IL 61299-5001 | 1 |
| COMMANDER<br>U.S. ARMY ARDEC<br>ATTN: AMSTA-AR-WEE, BLDG. 3022<br>　　　AMSTA-AR-AET-O, BLDG. 183<br>　　　AMSTA-AR-FSA, BLDG. 61<br>　　　AMSTA-AR-FSX<br>　　　AMSTA-AR-FSA-M, BLDG. 61 SO<br>　　　AMSTA-AR-WEL-TL, BLDG. 59<br>PICATINNY ARSENAL, NJ 07806-5000 | 1<br>1<br>1<br>1<br>1<br>2 | COMMANDER<br>U.S. ARMY TANK-AUTMV R&D COMMAND<br>ATTN: AMSTA-DDL (TECH LIBRARY)<br>WARREN, MI 48397-5000 | 1 |
| DIRECTOR<br>U.S. ARMY RESEARCH LABORATORY<br>ATTN: AMSRL-DD-T, BLDG. 305<br>ABERDEEN PROVING GROUND, MD<br>　21005-5066 | 1 | COMMANDER<br>U.S. MILITARY ACADEMY<br>ATTN: DEPT OF CIVIL & MECH ENGR<br>WEST POINT, NY 10966-1792 | 1 |
| DIRECTOR<br>U.S. ARMY RESEARCH LABORATORY<br>ATTN: AMSRL-WM-MB (DR. B. BURNS)<br>ABERDEEN PROVING GROUND, MD<br>　21005-5066 | 1 | U.S. ARMY AVIATION AND MISSILE COM<br>REDSTONE SCIENTIFIC INFO CENTER<br>ATTN: AMSAM-RD-OB-R (DOCUMENTS)<br>REDSTONE ARSENAL, AL 35898-5000 | 2 |
| COMMANDER<br>U.S. ARMY RESEARCH OFFICE<br>ATTN: TECHNICAL LIBRARIAN<br>P.O. BOX 12211<br>4300 S. MIAMI BOULEVARD<br>RESEARCH TRIANGLE PARK, NC 27709-2211 | 1 | COMMANDER<br>U.S. ARMY FOREIGN SCI & TECH CENTER<br>ATTN: DRXST-SD<br>220 7TH STREET, N.E.<br>CHARLOTTESVILLE, VA 22901 | 1 |

NOTE: PLEASE NOTIFY COMMANDER, ARMAMENT RESEARCH, DEVELOPMENT, AND ENGINEERING CENTER,
BENÉT LABORATORIES, CCAC, U.S. ARMY TANK-AUTOMOTIVE AND ARMAMENTS COMMAND,
　　AMSTA-AR-CCB-O, WATERVLIET, NY 12189-4050 OF ADDRESS CHANGES.